Met. Mater. Int., Vol. 23, No. 2 (2017), pp. 359~368
doi: 10.1007/s12540-017-6538-7

Dynamic Recrystallization Behavior and Constitutive Modeling of As-Cast 30Cr2Ni4MoV Steel Based on Flow Curves

Peng Zhou[1,2] and Qingxian Ma[1,2,*]

[1]Department of Mechanical Engineering, Tsinghua University, Beijing 100084, China
[2]Key Laboratory for Advanced Materials Processing Technology of Ministry of Education, Tsinghua University, Beijing 100084, China

(received date: 31 July 2016 / accepted date: 5 September 2016)

The compression deformation of 30Cr2Ni4MoV steel at different temperatures and strain rates is carried out on Gleeble 1500 thermal mechanical simulation tester. Based on the experimental flow curves, the strain hardening rate curves ($\theta = d\sigma/d\varepsilon$ versus σ) are derived, from which the characteristic stresses and strains are identified. Meanwhile, the dependences of the characteristic stresses and strains on Zener-Hollomon parameter are determined and the results show that the value of the critical stress of dynamic recrystallization is close to the value of the steady stress. With the aid of the experimental flow curves, the Avrami equation is employed to describe the kinetics of dynamic recrystallization. The time exponent (n) is expressed as a power law function of Zener-Hollomon parameter and the Avrami constant (k) is determined as a function of half of the time for the complete dynamic recrystallization (t_{50}). Furthermore, a constitutive model is presented based on the rule of mixtures when the dynamic recrystallization occurs. Validation of the constitutive model is implemented and the simulated results agree well with the experimental results.

Keywords: metals, compression test, thermomechanical processing, recrystallization, mechanical properties

1. INTRODUCTION

30Cr2Ni4MoV steel is widely used in ultra-super-critical power cycle generator production for its good property balance of strength, toughness and wear resistance. On account of the strict property requirement in the course of generator serving, it is necessary to precisely control the microstructure in the forging process. Limited by the large volume and quality, it is impossible to detect the microstructure evolution in time, so a systematic investigation including the stress performance, dynamic recrystallization (DRX) initiation, DRX kinetics model and the constitutive model is necessary for the quality control of the final product.

When the metal is subjected to plastic deformation at high temperature larger than half melting temperature, 0.5 T_m [1,2], DRX is the main approach of microstructure control and property improvement. Depending on the stacking fault energy (SFE) and deformation temperature [1], DRX is classified into discontinuous dynamic recrystallization (dDRX) and continuous dynamic recrystallization (cDRX). dDRX generally occurs during the hot deformation of metals, in which the dynamic recovery cannot take place with easy, with low to medium SFE [3-5]. On the other hand, in the high SFE metals, only cDRX operates when they are deformed at high temperature [6-8]. For the 30Cr2Ni4MoV steel used in this research, dDRX, which is characterized by a two-step process including nucleation and growth, takes place in the process of compression deformation at high temperature. Many researches have been carried out on the characteristic of dDRX in terms of flow curve appearance, dDRX initiation, microstructure evolution and recrystallization kinetics model [9-20]. Typical appearance of flow curves of dDRX is obtained and the effects of temperature, strain rate and grain size on the appearance of the flow curves are discussed [9-11]. Based on the experimental flow curve, the work hardening rate curve is derived and the characteristic points are identified from the work hardening curve. It has been pointed out that the characteristic stresses and strains, which include the yield stress (σ_0), the critical stress (σ_c) and strain (ε_c) of dDRX, the peak stress (σ_p) and strain (ε_p) of dDRX, the steady stress (σ_s) and the saturation stress (σ_{sat}) of DRV, can be expressed as functions of temperature and strain rate [12-16]. Furthermore, the microstructure evolution of dDRX that the nuclei initially appear along the original grain boundaries followed by the nuclei growth is investigated [1,2,16]. Combining with the flow curves obtained in the experiment, the Avrami relation which is widely used in the description of static recrystallization (SRX) is employed to determine the kinetics model of dDRX. [13,14,16-20]. In the case of constitutive modeling, the hyperbolic sine-typed

*Corresponding author: maqxdme@mail.tsinghua.edu.cn

Arrhenius equation is widely employed in metals and alloys [13,15].

In recent years, many researchers have investigated the hot deformation behavior of the 30Cr2Ni4MoV steel. While studying the dDRX and meta-dynamic recrystallization (mDRX), Chen *et al.* discussed the effects of strain rate, temperature and initial grain size [21,22]. Liu studied the microstructure evolution of 30Cr2Ni4MoV steel during multi-pass hot deformation [23]. Nevertheless, the dependences of characteristic points mentioned above on the temperature and strain rate have not been discussed and no constitutive model is proposed.

In this article, the characteristic stresses and strains are identified from the strain hardening curves which are derived from the experimental flow curves. The dependences of the above characteristic stresses and strains on temperature and strain rate are discussed. Besides of that, the kinetics model of DRX is determined and both the time exponent and the Avrami constant are expressed as functions of temperature and strain rate. With the aid of the DRX kinetics model, a new constitutive modeling method is proposed and the validation of this model is implemented. It is shown that the simulated results agree well with the experimental results.

2. EXPERIMENT PROCEDURE

The 30Cr2Ni4MoV steel used in this research was directly sampled from 600t ingot with a composition of 0.28C-0.02Mn-0.01Si-0.003P-0.003S-1.72Cr-0.41Mo- 3.63Ni-0.11V- (bal.) Fe, all values given in wt%. Compression specimens 12 mm in length and 8 mm in diameter were machined.

The machined cylinder samples were compressed on Gleeble-1500 thermal mechanical simulation tester with Ta piece between sample head and punch head to minimize the friction and avoid the sticking problem. In order to realize the same initial grain size and homogeneous microstructure, the specimens were firstly reheated to 1200 °C for 5 min [24]. The initial austenite grain size is 196 μm as shown in Fig. 1. After the structure uniformity, the samples were cooled to the deformation temperature and compressed to a strain of 0.7. The details of the design of experiment are shown in Table 1.

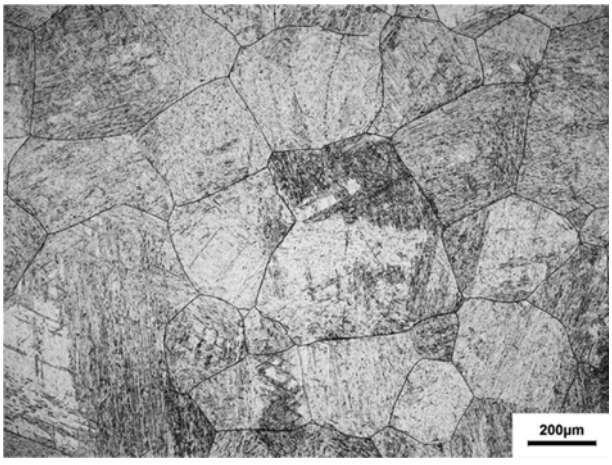

Fig. 1. Austenite microstructure after reheating at 1200 °C and 5 min soaking.

Table 1. Design of experiment pertaining to the 30Cr2Ni4MoV steel

T (°C)	$\dot{\varepsilon}$ (s^{-1})
1200, 1150	0.01, 0.1, 0.25, 0.5, 1
1100, 1050	0.01, 0.1, 0.25, 0.5
1000	0.01, 0.1

3. RESULTS AND DISCUSSION

3.1. Flow curves of hot compression deformation

The experimental flow curves are fitted with a seventh order polynomial and smoothed from the yield strain (ε_0) which is identified on the flow curve in terms of a 2% offset (removing the elastic deformation) in the total strain [20]. The corresponding stress to yield strain is the yield stress (σ_0). Figure 2 shows an example of experimental flow curve together with its fitted and smoothed curve.

When the 30Cr2Ni4MoV steel is subjected to compression deformation at elevated temperature higher than 0.5 T_m, the DRX is the main softening mechanism once the stress exceeds the critical stress of DRX [1,2,25], σ_c. Typical experimental flow curves are shown in Fig. 3. It is clearly that the stress increases with the increasing strain and the work hardening rate gradually decreases, which is caused by the occurrence of DRX and DRV, until there is a significant peak, σ_p. Then the stress decreases with increasing strain until the steady stress (σ_s), which can be identified as the balance between work hardening and dynamic softening, is attained.

The effect of the strain rate on the appearance of the flow

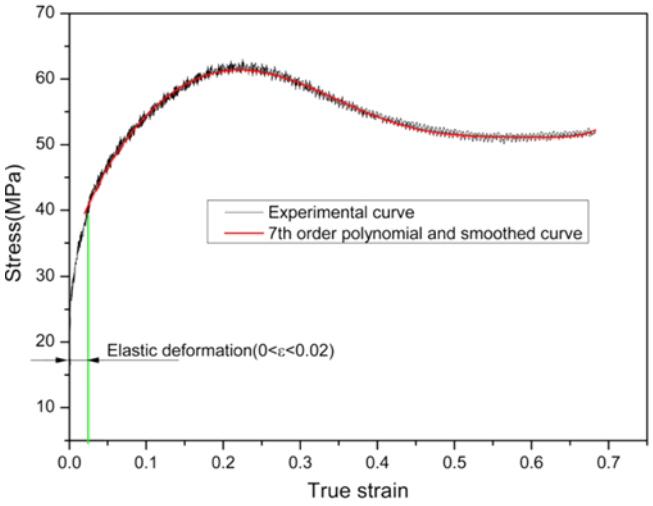

Fig. 2. An example of experimental flow curve together with its fitted and smoothed curve.

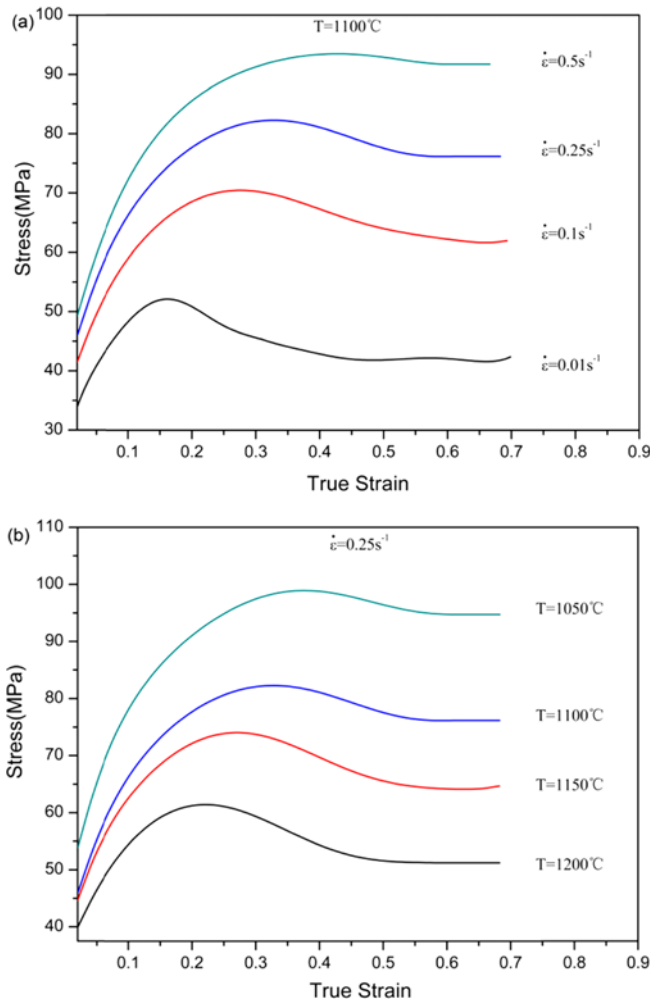

Fig. 3. Typical flow curves under different deformation conditions: (a) the effect of strain rate on the flow stress, T = 1100 °C; (b) the influence of temperature on the flow stress, $\dot{\varepsilon}$ = 0.25 s^{-1}.

curves is illustrated in Fig. 3(a) and the influence of the temperature on the flow stress is shown in Fig. 3(b). It is obviously that the flow stress is affected by both the deformation temperature and strain rate, which are combined in the Zener-Hollomon parameter expressed by Eq. (1) [1].

$$Z = \dot{\varepsilon}\exp(Q/RT) \tag{1}$$

where $\dot{\varepsilon}$ is the strain rate, T is the temperature, R is the gas constant that equals to 8.314 Jmol^{-1} K^{-1} in this study and Q is the activation energy which is calculated with the method mentioned in Ref [13,15]. The value of Q is equal to 374.92 kJ/mol.

The behavior of the flow stress appearance can be attributed to the competition between the strain hardening and dynamic softening resulted from DRV and DRX. When the steel is compressed at high temperature and low strain rate, it is easy for the dislocation climb and cross-slip, as well as the grain boundary mobility, which makes it more possible for the occurrence DRV and DRX. So the flow stress decreases with the increasing temperature and decreasing strain rate. On the contrary, low temperature and high strain rate restrain the growth of DRX grains and enhance the work hardening effect. Thus, the flow stress increases accordingly.

3.2. Characteristic stresses and strains

3.2.1. Characteristic stresses and strains identification

When the DRV and DRX take place, there are some characteristic points which include the yield stress (σ_0), the critical stress (σ_c) and strain (ε_c) of DRX, the peak stress (σ_p) and strain (ε_p) of DRX, the steady stress (σ_s) and the saturation stress (σ_{sat}) of DRV. The plot of strain hardening rate with respect to stress ($\theta = d\sigma/d\varepsilon$ versus σ), derived from the fitted and smoothed flow curve, is employed to determine the above stresses and strains in this study [15,20,25]. Figure 4 shows an example of θ–σ curve together with the characteristic points when the strain rate is 0.25 s^{-1} at 1100 °C. At the initial stage of the deformation, the work hardening rate decreases with the increasing stress until the inflection point, which can be identified as σ_c, is attained. Then the work hardening rate drops more rapidly, which is resulted from the occurrence of the DRX, to zero. The corresponding stress represents σ_p. With further increasing strain, the work hardening rate continues to drop to the minimum and then increase to zero again, which implies that the σ_s is attained. Additionally, the dash line extrapolated from the linear part before σ_c is assumed as the work hardening rate caused by DRV alone. When the assumed work hardening rate reaches zero, the σ_{sat} is attained. As long as the σ_c and σ_p are determined, the corresponding strains (ε_c and ε_p) can be identified from the flow curves.

As outlined above, it is important to accurately identify σ_c for the determination of σ_{sat}. Various models have been proposed to predict the initiation of DRX [25-28]. In this research,

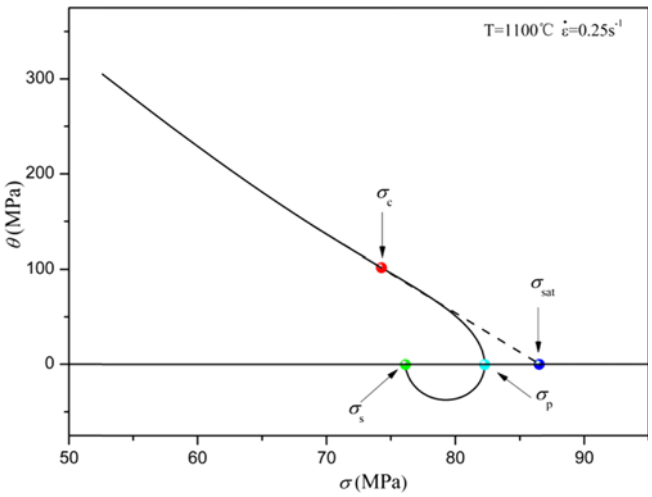

Fig. 4. Work hardening rate with respect to stress: determination of σ_c, σ_p, σ_s and σ_{sat}.

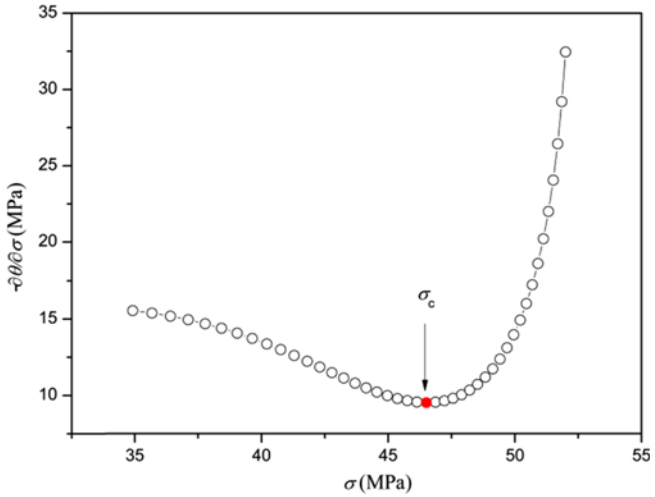

Fig. 5. An example of the critical stress of DRX identification (T = 1100 °C, $\dot{\varepsilon}$ = 0.01 s^{-1}).

the method proposed by Poliak and Jonas in 1996 [25] is used on account of it's widely application without the limitation of strain rate [29] and testing mode, i.e. tension, compression and torsion [30]. Three steps are involved in the σ_c determination: firstly measuring the work hardening rate ($\theta = \partial\sigma/\partial\varepsilon$), then taking the derivative of θ with respect to stress ($\partial\theta/\partial\sigma$) and finally plotting the negative value of $\partial\theta/\partial\sigma$ versus stress. The inflection in the curve, the local minimum, indicates the initiation of DRX. Figure 5 shows an example of $(-\partial\theta/\partial\sigma)-\sigma$ diagram when the deformation temperature is 1100 °C with a strain rate of 0.01 s^{-1}. With the method described above, all the characteristic stresses and strains are calculated and listed in Table 2.

3.2.2. Critical strain and peak strain of DRX

With the method described above, typical $(-\partial\theta/\partial\sigma)-\sigma$ plots for the determination of σ_c at different deformation conditions are shown in Fig. 6. The effects of deformation temperature and strain rate on σ_c are illustrated in 6(a) and (b), respectively. It is found that the σ_c increases with the decreasing temperature and increasing strain rate, i.e. low value of Z. So it is reasonable that the ε_c, as well as the ε_p, can be described as a function of Z, [12,31].

Figure 7 shows the plots of the ε_c and ε_p versus Z. By regression analysis, the dependences of ε_c and ε_p on Z can be expressed as Eqs. (2) and (3), respectively.

$$\varepsilon_c = 1.07 * 10^{-3} * Z^{0.158} \quad (2)$$

$$\varepsilon_p = 1.38 * 10^{-3} * Z^{0.173} \quad (3)$$

Furthermore, it has been pointed out that the relationship between ε_c and ε_p can be described as follows [32,33]:

$$\varepsilon_c = C\varepsilon_p \quad (4)$$

where C is the constant. By substituting the values of ε_c and ε_p as listed in Table 2 into Eq. (4) and regression analysis (Fig. 8), the value of C is calculated to be equal to 0.49. The value of C is located in the range reported previously for steels which is between 0.3 to 0.9 [20,33-37]. Therefore, the relationship between ε_c and ε_p can be expressed as follows:

$$\varepsilon_c = 0.49\varepsilon_p \quad (5)$$

Table 2. Values of characteristic strains and stresses at different deformation conditions

T (°C)	$\dot{\varepsilon}$ (s^{-1})	ε_c	ε_p	σ_0 (MPa)	σ_c (MPa)	σ_p (MPa)	σ_s (MPa)	σ_{sat} (MPa)
1200	0.01	0.06	0.11	28	35	38	35	42
	0.1	0.1	0.18	36	48	52	40	59
	0.25	0.12	0.22	39	56	62	51.2	69
	0.5	0.13	0.26	41	62	69	59	75
	1	0.15	0.31	41	63	77	65.5	86
1150	0.01	0.065	0.13	32	40	45	40	53
	0.1	0.1	0.23	40	55	62	51	72
	0.25	0.13	0.27	44	66	74	64	80
	0.5	0.15	0.31	45	71	79	69	85
	1	0.17	0.34	48	80	86	83	91
1100	0.01	0.09	0.18	31.5	46.5	53	42.5	61
	0.1	0.13	0.28	41.5	64	75	63	80
	0.25	0.16	0.33	46	74	82	76	89
	0.5	0.19	0.38	49	88.5	93	90	97
1050	0.01	0.12	0.21	36	57.5	64	52.5	73
	0.1	0.16	0.33	51	81	90	81	97
	0.25	0.2	0.38	54	91	99	86	104
	0.5	0.2	0.45	61	100	110	102	115
1000	0.01	0.14	0.25	45	70	79	65	87
	0.1	0.19	0.42	56	95	106	95	111

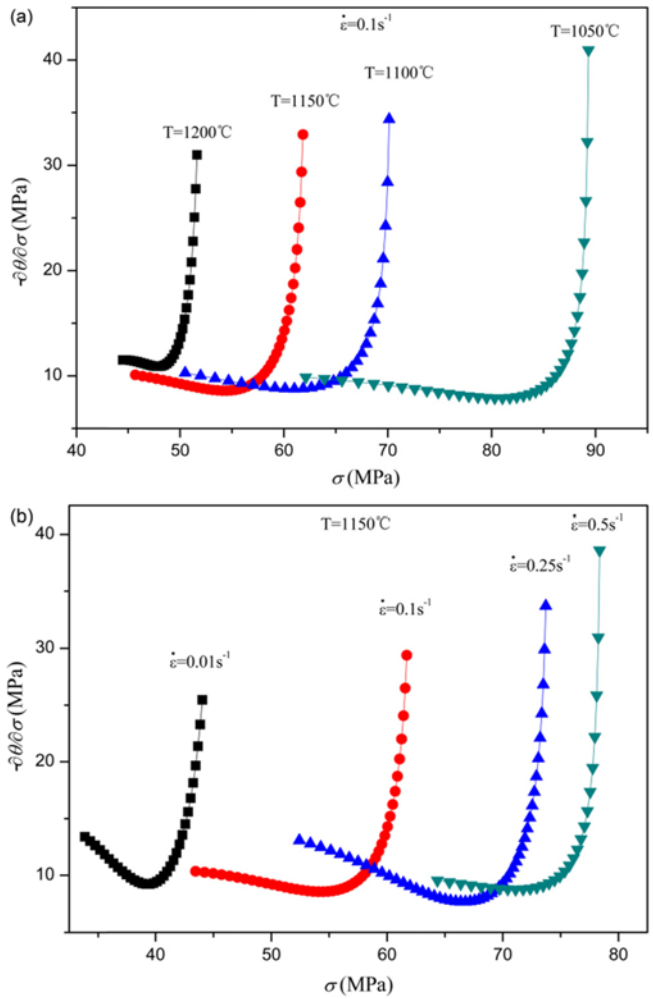

Fig. 6. Typical determination of σ_c at different deformation conditions: (a) the effect of temperature on σ_c, $\dot{\varepsilon}$ = 0.1 s^{-1}; (b) the influence of strain rate on σ_c, T = 1150 °C.

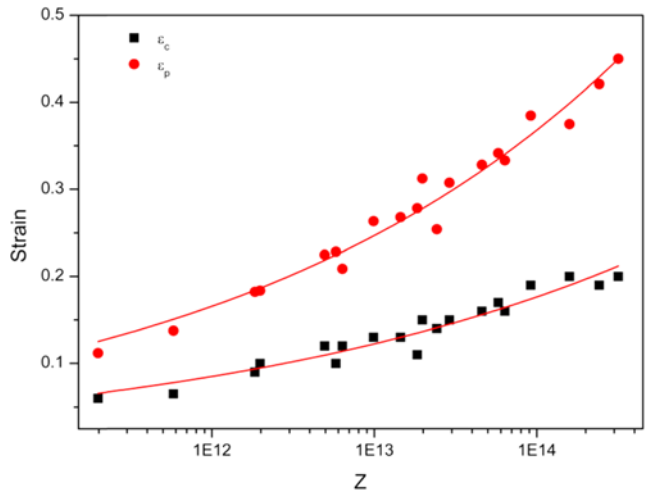

Fig. 7. The dependence of ε_c and ε_p on Z.

3.2.3. Characteristic stresses (σ_0, σ_c, σ_p, σ_s and σ_{sat})

Jorge Jr. and Balancin proposed that the mechanical parameters can be described by a simple power-law equation with respect to Z [38]. Figure 9(a) shows the dependences of σ_0, σ_c, σ_p and

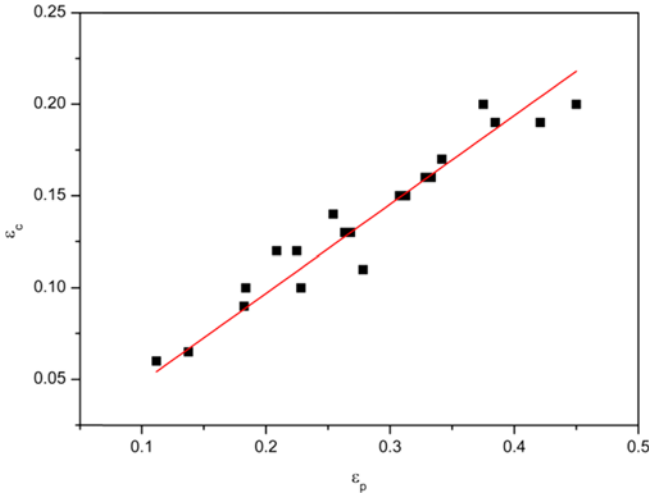

Fig. 8. Relationship between ε_c and ε_p.

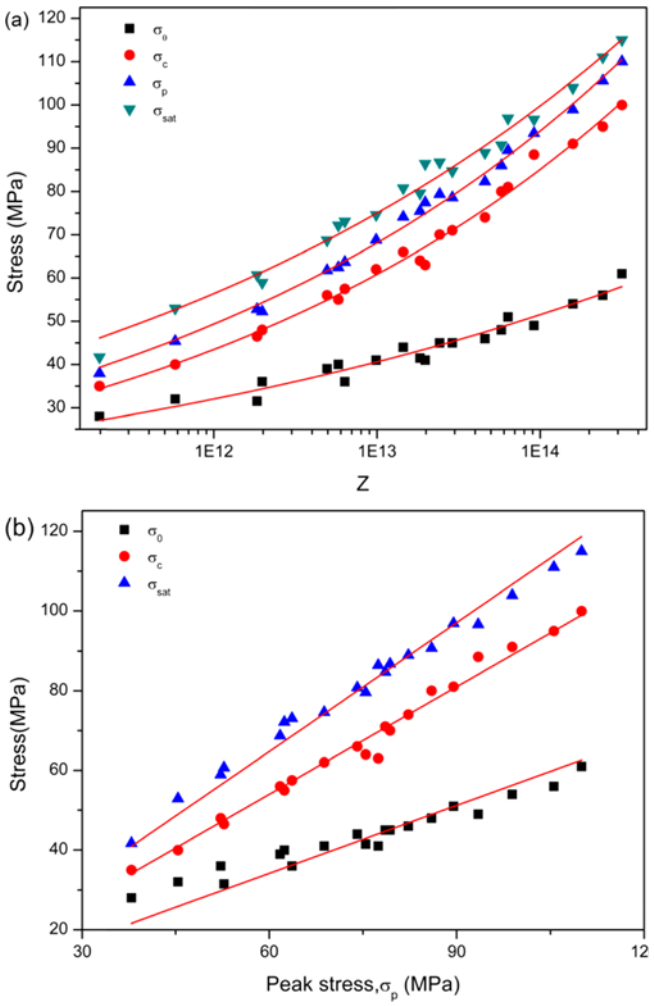

Fig. 9. (a) The dependence of σ_0, σ_c, σ_p and σ_{sat} on Z; (b) Dependence of σ_0, σ_c, and σ_{sat} on σ_p.

σ_{sat} on Z. By regression analysis, the following equations are developed:

$$\sigma_c = 1.85 * Z^{0.10} \quad (6)$$

$$\sigma_c = 0.78 * Z^{0.15} \quad (7)$$

$$\sigma_p = 1.03 * Z^{0.14} \quad (8)$$

$$\sigma_{sat} = 1.84 * Z^{0.12} \quad (9)$$

For modeling purpose, Jonas *et al.* studied the dependences of σ_0, σ_c, σ_s and σ_{sat} on σ_p, as the latter is more readily measurable. They found that the derived quantities of σ_0, σ_c, σ_s and σ_{sat} can be able to express as ratios of σ_p [20]. As shown in Fig. 9(b), the values of σ_0, σ_c, and σ_{sat} are expressed as ratios of σ_p and The following equations give a good fit to the data:

$$\sigma_0 = 0.57\sigma_p \quad (10)$$

$$\sigma_c = 0.90\sigma_p \quad (11)$$

$$\sigma_{sat} = 1.08\sigma_p \quad (12)$$

Additionally, the relationship between σ_s and σ_c is discussed in this study as shown in Fig. 10. By regression analysis, the relationship can be expressed as follows:

$$\sigma_s = 0.99\sigma_c \quad (13)$$

It is of interest that the coefficient is close to one. The DRX begins to occur when the stress reaches σ_c and the DRX is accomplished when the σ_s is attained. From the relation between σ_s and σ_c, it can be concluded that the DRX cannot take place in the recrystallized grains unless the stress is higher than σ_c. In other words, the σ_c can be considered as the saturation stress of the recrystallized grains.

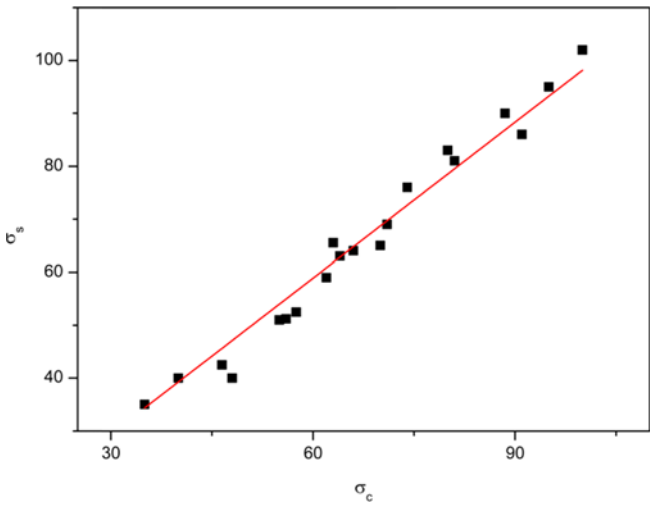

Fig. 10. The relationship between σ_s and σ_c.

3.3. DRX kinetics

It has been pointed out that the DRX takes place when the stress is larger than the σ_c in a sigmoidal manner [1,2], which include incubation period, acceleration and steady stage. Usually, the Avrami equation is used to describe the kinetics of DRX as follows [20,39,40]:

$$X_{drx} = 1 - \exp(-kt^n) = 1 - \exp(-k((\varepsilon - \varepsilon_c)/\dot{\varepsilon})^n) \quad (14)$$

Here X_{drx} is the volume fraction of DRX, k is the Avrami constant and n is the time exponent. In order to finally determine the X_{drx}, the dependences of k, n and ε_c on temperature and strain rate are necessary. The ε_c has been expressed as a function of Z as described in Sec. 3.2.2.

Taking the logarithm of both sides of Eq. (14), it leads to:

$$\ln[\ln(1/(1-X_{drx}))] = lnk + nlnt \quad (15)$$

As long as the X_{drx} can be determined, the values of k and n can be calculated by regression analysis from $X_{drx} = 0.1$ to $X_{drx} = 0.9$ as shown in Fig. 11 [20]. The X_{drx} can be calculated by either metallographic measurement or flow curve analysis. Since the austenite is not stable at room temperature for 30Cr2Ni4MoV steel [24], it is difficult to observe the microstructure evolution by metallographic measurement. Therefore, the X_{drx} is obtained from the flow curves analysis in this research.

When the 30Cr2Ni4MoV steel is deformed at high temperature, DRV and DRX take place simultaneously as the softening mechanism. As pointed out in Ref. [40], the stress can be expressed using the rule of mixtures when the DRX occurs:

$$\sigma = (1 - X_{drx})\sigma_{wh} + \overline{\sigma}_{rex} X_{drx} \quad (16)$$

Here σ is the stress of the deformed steel, σ_{wh} is the stress pertaining to the work hardening grains and $\overline{\sigma}_{rex}$ is the average

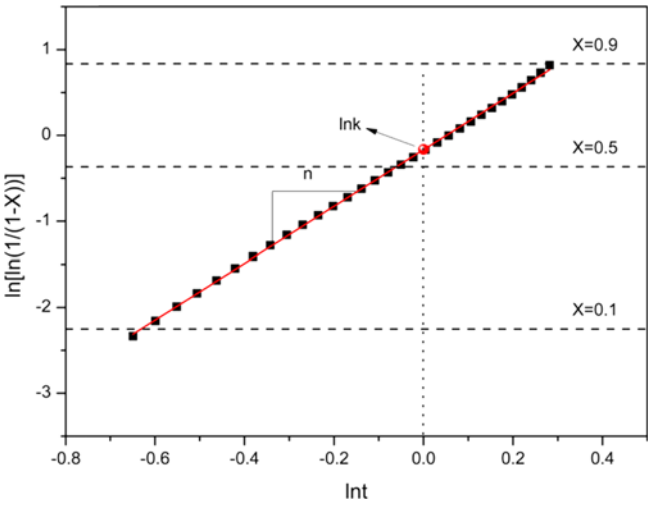

Fig. 11. Determination of the value of n and k from the Avrami plot using the range of X_{drx} between $X_{drx} = 0.1$ to $X_{drx} = 0.9$.

Table 3. The values of r and r' at different deformation conditions

T (°C)	$\dot{\varepsilon}$ (s^{-1})	r	r'
1200	0.01	13.72	19.50
	0.1	7.90	11.90
	0.25	7.50	11.29
	0.5	7.34	10.62
	1	6.22	9.15
1150	0.01	8.74	15.31
	0.1	6.00	10.32
	0.25	6.96	10.42
	0.5	6.90	9.82
	1	6.48	8.33
1100	0.01	7.84	13.36
	0.1	6.08	10.69
	0.25	6.36	9.18
	0.5	7.16	8.54
1050	0.01	7.08	9.22
	0.1	7.28	11.76
	0.25	6.20	8.88
	0.5	6.26	8.17
1000	0.01	7.38	8.96
	0.1	7.66	11.76

stress of the grains in which DRX has taken place. Therefore, X_{drx} can be calculated by converting Eq. (16) into the following form:

$$X_{drx} = (\sigma_{wh} - \sigma)/(\sigma_{wh} - \overline{\sigma}_{rex}) \tag{17}$$

The σ_{wh} and $\overline{\sigma}_{rex}$ can be expressed as follows [39,40]:

$$\sigma_{wh} = \sigma_{sat} - (\sigma_{sat} - \sigma_0)\exp(-r(\varepsilon - \varepsilon_0)) \tag{18}$$

$$\overline{\sigma}_{rex} = \sigma_c - (\sigma_c - \sigma_0)\exp(-r'(\varepsilon - \varepsilon_0)) \tag{19}$$

where r and r' are the work hardening rate pertaining to the work hardening grains and dynamic recrystallized grains, respectively. The values of r and r' can be calculated from the $2\theta\sigma$–σ^2 plots which are derived from the experimental flow stress curves. The specific method can be found in X. Quelennec's work [40]. All the values of r and r' at different deformation conditions are determined and listed in Table 3. Figure 12 schematically illustrates the curves of σ_{wh}, $\overline{\sigma}_{rex}$ and experimental flow curve (σ_{exp}) at a certain deformation condition. With the aid of the above three stress curves, the values of X_{drx} at different deformation conditions can be calculated. By substituting the values of X_{drx} into Eq. (15) and linear regression analysis, we obtain the values of k and n at different deformation conditions as listed in Table 4. Figure 13 shows a series of typical $\ln[\ln(1/(1-X_{drx}))]$-*int* plots at different deformation conditions.

The values of n at different deformation conditions with respect to Z are illustrated in Fig. 14. By power regression,

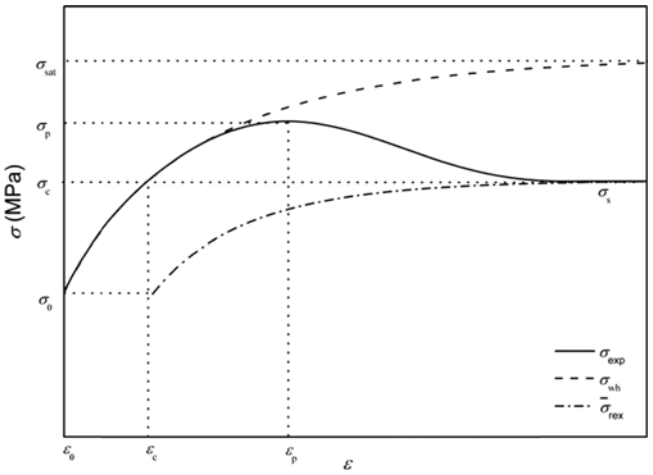

Fig. 12. Schematic diagram of an experimental stress (σ_{exp}), work hardening stress (σ_{wh}) and average dynamic recrystallization stress ($\overline{\sigma}_{rex}$ evolution with respect to strain.

Table 4. The values of n and k at different deformation conditions

T (°C)	$\dot{\varepsilon}$ (s^{-1})	n	k
1200	0.01	3.900	0.00018
	0.1	3.402	0.26100
	0.25	3.131	2.41778
	0.5	3.272	9.04634
	1	2.971	37.21791
1150	0.01	3.431	0.00015
	0.1	3.106	0.08350
	0.25	3.316	0.84967
	0.5	3.123	5.15244
	1	2.807	18.15725
1100	0.01	3.216	0.00011
	0.1	2.874	0.06910
	0.25	3.037	0.46134
	0.5	2.949	1.88859
1050	0.01	2.959	0.00009
	0.1	3.006	0.02927
	0.25	2.594	0.28383
	0.5	2.700	0.95000
1000	0.01	3.043	0.00008
	0.1	2.606	0.01625

the n can be expressed as a function of Z.

$$n = 12.026 * Z^{-0.045} \tag{20}$$

In the case of k simulation, it is much more complex in comparison with n. In this study, the t_{50}, half of time for complete dynamic recrystallization, is employed which can be expressed as follows [20]:

$$t_{50} = A d_0^{v} \exp(Q_{drx}/RT) * \dot{\varepsilon}^{-q} \tag{21}$$

Here A is the material constant, d_0 is the initial grain size, v

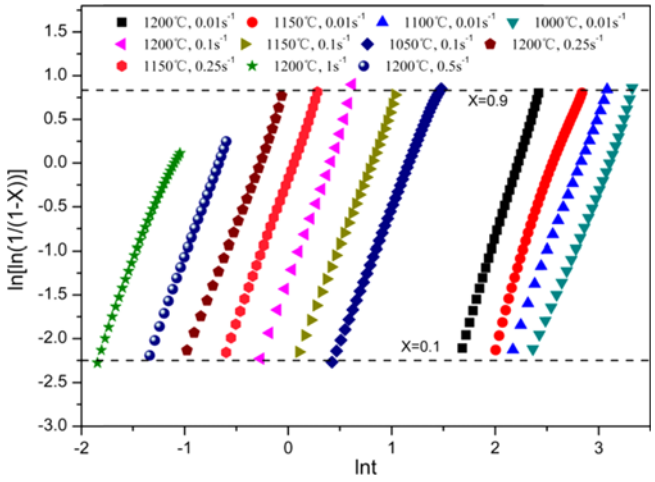

Fig. 13. Typical plots of $\ln[\ln(1/(1-X_{drx}))]$ -*int* at different deformation conditions.

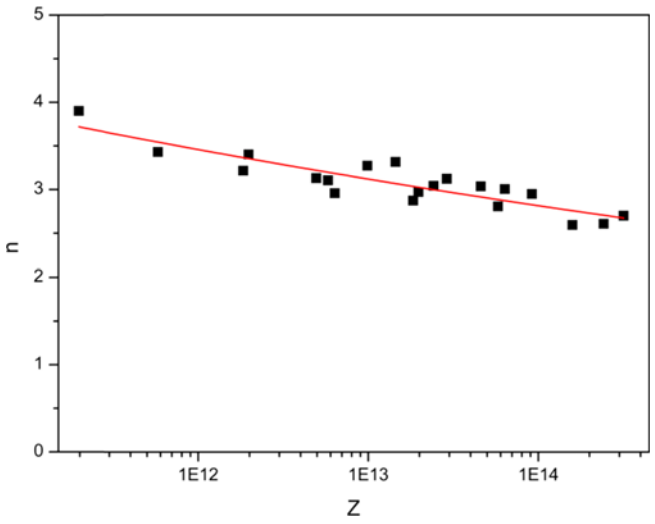

Fig. 14. Dependence of n on Z of the 30Cr2Ni4MoV steel.

is the grain size exponent, q is the strain rate exponent and Q is the activation energy associated with DRX mentioned above.

In view of the $Ad_0^{-v}\exp(Q_{drx}/RT)$ and q in Eq. (21) is constant when the temperature is fixed [20], t_{50} can be regarded as a power-law function of $\dot{\varepsilon}$. The values of t_{50} at different deformation conditions can be obtained from the $\ln[\ln(1/(1-X_{drx}))]$ -*int* plots when the X_{drx} is equal to 0.5. Figure 15(a) shows the dependence of t_{50} on $\dot{\varepsilon}$ at different deformation temperatures. The values of $Ad_0^{-v}\exp(Q_{drx}/RT)$ and $-q$ can be obtained from the pre-exponential factor and the exponent, respectively. The dependence of deformation conditions can be obtained from the $Ad_0^{-v}\exp(Q_{drx}/RT)$ on temperature is illustrated in Fig. 15(b). Figure 15(c) shows the dependence of $-q$ on temperature. By linear regression, the dependences of $Ad_0^{-v}\exp(Q_{drx}/RT)$ and $-q$ on temperature can be obtained as follows:

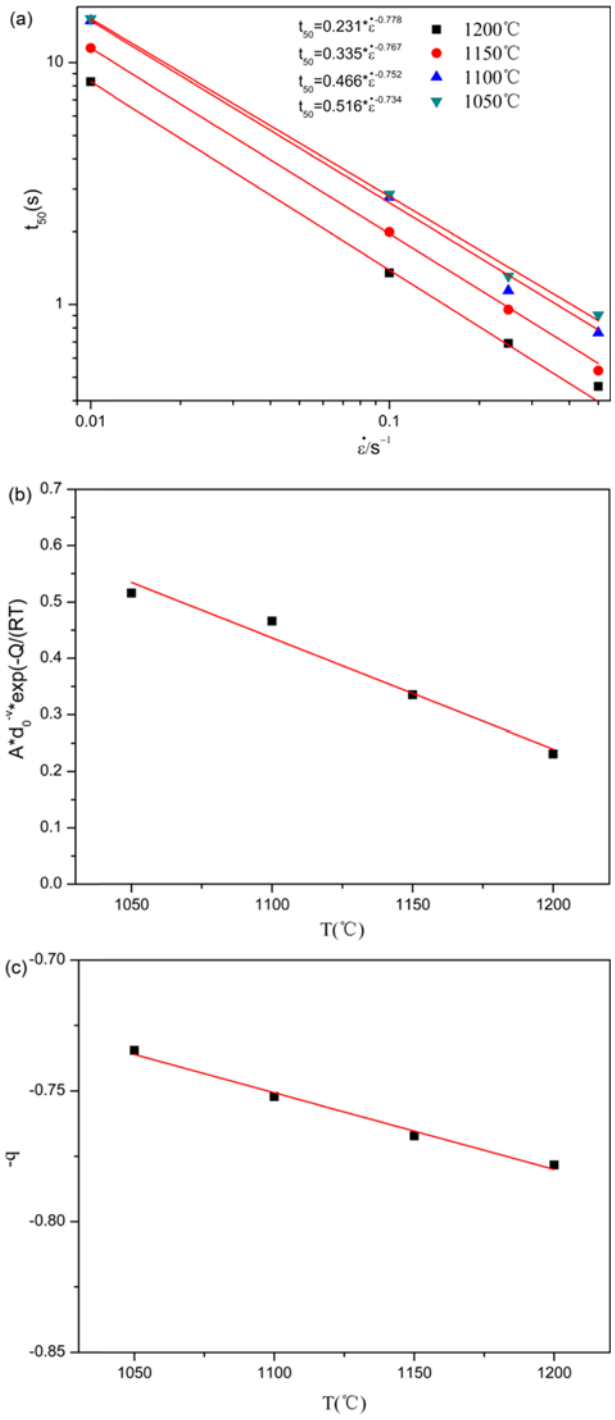

Fig. 15. (a) The dependence of t_{50} on strain rate at four different deformation temperatures; (b) Dependence of pre-exponential factor ($Ad_0^{-v}\exp(Q_{drx}/RT)$) of t_{50} on deformation temperature; (c) Dependence of $-q$ on deformation temperature.

$$Ad_0^{-v}\exp(Q_{drx}/RT) = -1.97*10^{-3}*T+2.60 \quad (22)$$

$$-q = -2.93*10^{-4}*T-0.43 \quad (23)$$

Then the k can be expressed as Eq. (24):

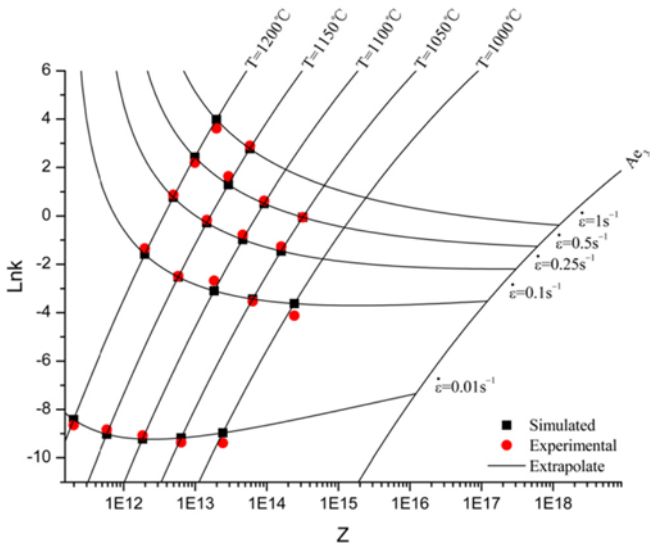

Fig. 16. Comparison between the values of k obtained from experiment and simulation.

$$k = 0.693/t_{50}^{n} \tag{24}$$

In order to verify the accuracy of the simulated values of k, the comparison between the experimental ks and predicted ks is illustrated in Fig. 16. It is shown that the predicted values of k agree well with the experimental values of k. It should be pointed out that the extrapolated values of k are also shown in Fig. 16 when the deformation temperature is above *Ae3* (810 °C) [24].

Till now, all the parameters needed for the determination of X_{drx} have been expressed as functions of deformation temperature and strain rate. It should be noted that the peak strain ε_p is absence in Eq. (25). So it is possible to predict the dynamic recrystallization fraction as long as the strain reaches the critical strain.

$$X_{drx} = 1 - \exp\left\{-\left[\frac{0.693}{(-1.97*10^{-3}*T+2.60)*\dot{\varepsilon}^{(-2.93*10^{-4}*T-0.43)}}\right]*\left(\frac{\varepsilon-(1.07*10^{-3}*Z^{0.158})}{\dot{\varepsilon}}\right)^{12.026*Z^{-0.045}}\right\} \tag{25}$$

3.4. Construction of constitutive model

As described by Eq. (16), as long as the σ_{wh}, $\overline{\sigma}_{rex}$ and X_{drx} can be expressed as functions of temperature, strain rate and strain, the constitutive model of 30Cr2Ni4MoV steel can be obtained. In Sec. 3.3, the X_{drx} has been expressed as a function of temperature, strain rate and strain (Eq. (25)). The dependences of σ_{sat}, σ_0, σ_c, and ε_c on temperature and strain rate has been obtained in Sec. 3.2. Provided the r and r' can be described as functions of temperature and strain rate, the σ_{wh} and $\overline{\sigma}_{rex}$ can be expressed as functions of temperature, strain rate and strain. The values of r and r' at different deformation conditions have been determined as shown in Table 4 and all the values are plotted in Fig. 17 with respect to Z. The data can be fitted as follows:

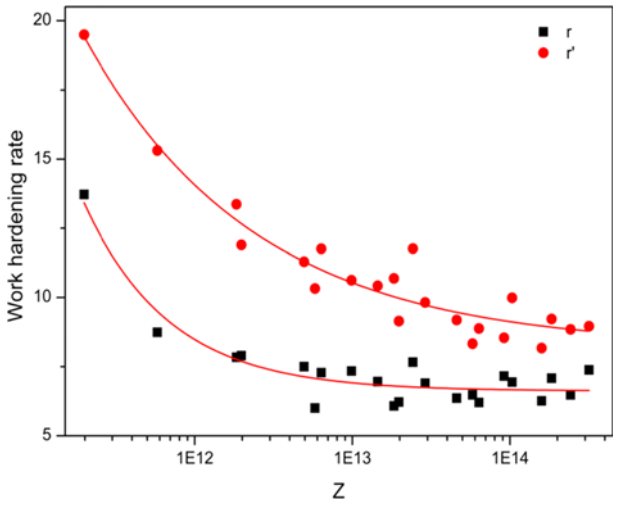

Fig. 17. The dependence of r and r' on Z.

$$r = 6.619 + 7.4*10^{9}*Z^{-0.8} \tag{26}$$

$$r' = 8.196 + 3.7*10^{5}*Z^{-0.4} \tag{27}$$

Till now, all the parameters needed for the determination of the constitutive model of 30Cr2Ni4MoV has been expressed as functions of temperature, strain rate and strain. In order to validate the accuracy of the constitutive model, the comparison between the simulated stress and the experimental stress is implemented as shown in Fig. 18. It can be seen that the model results agree well with the experimental flow curves.

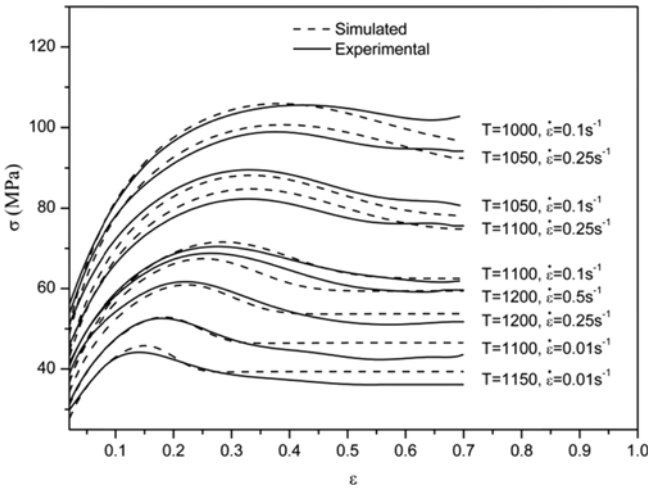

Fig. 18. Comparison between simulated flow stress and experimental flow curves.

4. CONCLUSION

The hot deformation of 30Cr2Ni4MoV steel has been carried out in order to investigate the DRX behavior and construct the constitutive model. All the characteristic stresses and strains identified from the work hardening rate curves are expressed as functions of Z parameter. It is of interest that the values of σ_s are close to σ_0. By combining the Avrami equation with the stress loss resulted from the DRX, the kinetics model of DRX, in which the ε_p is absence, is determined. Based on the kinetics model of DRX and the obtained characteristic stresses and strains, the constitutive model of 30Cr2Ni4MoV steel during hot deformation is established. It is shown that the predicted results are in good agreement with the experimental results.

ACKNOWLEDGEMENT

The authors gratefully acknowledge financial support from National Basic Research Program of China (2011CB012903).

REFERENCES

1. T. Sakai, A. Belyakov, R. Kaibyshev, H. Miura, and J. J. Jonas, *Prog. Mater. Sci.* **60**, 130 (2014).
2. R. D. Doherty, D. A. Hughes, F. J. Humphreys, J. J. Jonas, D. Juul Jensen, M. E. Kassner, *et al. Mat. Sci. Eng. A* **238**, 219 (1997).
3. T. Maki, K. Akasaka, K. Okuno, and I. Tamura, *ISIJ Int.* **22**, 253 (1982).
4. T. Sakai, *J. Mater. Process. Tech.* **53**, 349 (1995).
5. T. Sakai and M. Ohashi, *Mater. Sci. Technol.* **6**, 1251 (1990).
6. Q. Liu, X. Huang, M. Yao, and J. Yang, *Acta Mater.* **40**, 1753 (1992).
7. K. Tsuzaki, X. X. Huang, and T. Maki, *Acta Mater.* **44**, 4491 (1996).
8. S. Gourdet and F. Montheillet, *Acta Mater.* **51**, 2685 (2003).
9. C. M. Sellars, *Philos. T. Roy. Soc. A* **288**, 147 (1978).
10. H. J. Mcqueen and J. J. Jonas, *Treatise Mater. Sci. Technol.*, Vol. 6 (ed. R. J. Arsenault), pp.393-493, Academic Press, New York, USA (1975).
11. B. Derby, *Acta Mater.* **39**, 955 (1991).
12. S. Naghdy and A. Akbarzadeh, *Mater. Design* **53**, 910 (2014).
13. G. Z. Quan, A. Mao, G. C. Luo, J. T. Liang, D. S. Wu, and J. Zhou, *Mater. Design* **52**, 98 (2013).
14. X. M. Chen, Y. C. Lin D. X. Wen, J. L. Zhang, and M. He, *Mater. Design* **57**, 568 (2014).
15. C. Zhang, L.W. Zhang, W. F. Shen, C. R. Liu, Y. N. Xia, and R.Q. Li, *Mater. Design* **90**, 804 (2016).
16. A. I. Fernández, P. Uranga, B. López, and J. M. Rodriguez-Ibabe, *Mat. Sci. Eng. A* **361**, 367 (2003).
17. H. J. McQueen, *Mat. Sci. Eng. A* **387-389**, 203 (2004).
18. G. R. Stewart, A. M. Elwazri, S. Yue, and J. J. Jonas, *Mater. Sci. Technol*. **22**, 519 (2006).
19. J. Wang, J. Chen, Z. Zhao, and X. Y. Ruan, *J. Iron Steel Res. Int.* **15**, 78 (2008).
20. J. J. Jonas, X. Quelennec, L. Jiang, and E. Martin, *Acta Mater.* **57**, 2748 (2009).
21. F. Chen, Z. S. Cui, D. S. Sui, and B. Fu, *Mat. Sci. Eng. A* **540**, 46 (2012).
22. F. Chen, Z. S. Cui, and S. J. Chen, *Mat. Sci. Eng. A* **528**, 5073 (2011).
23. X. Liu, *Ph. D. Thesis*, pp.22-38, Tsinghua University, Beijing (2010).
24. R. K. Chen, *Ph. D. Thesis*, pp.36-51, Shanghai Jiao Tong University, Shanghai (2012).
25. E. I. Poliak and J. J. Jonas, *Acta Mater.* **44**, 127 (1996).
26. M. R. Barnett, G. L. Kelly, and P. D. Hodgson, *Metall. Mater. Trans. A* **33**, 1893 (2002).
27. G. Gottstein, M. Frommert, M. Goerdeler, and N. Schafer, *Mat. Sci. Eng. A* **387-389**, 604 (2004).
28. H. Mirzadeh and A. Najafizadeh, *Mater. Design* **31**, 1174 (2010).
29. E. I. Poliak and J. J. Jonas, *ISIJ Int.* **43**, 684 (2003).
30. J. J. Jonas and E. I. Poliak, *Mater. Sci. Forum* **426-432**, 57 (2003).
31. Y. G. Liu, M. Q. Li, and J. Luo, *Mat. Sci. Eng. A* **574**, 1 (2013).
32. M. S. Chen, Y. C. Lin, and X. S. Ma, *Mat. Sci. Eng. A* **556**, 260 (2012).
33. E. Anelli, *ISIJ Int.* **32**, 440 (1992).
34. A. Kirihata, F. Siciliano, T. M. Maccagno, and J. J. Jonas, *ISIJ Int.* **38**, 187 (1998).
35. F. Siciliano and J. J. Jonas, *Metall. Mater. Trans. A* **31**, 511 (2000).
36. H. Mirzadeh and A. Najafizadeh, *Mater. Design* **31**, 1174 (2010).
37. H. Mirzadeh and A. Najafizadeh, *ISIJ Int.* **53**, 680 (2013).
38. A. M. Jorge Junior and O. Balancin, *Mater. Res.* **8**, 309 (2005).
39. X. Quelennec, N. Bozzolo, J. J. Jonas, and R. Logé, *ISIJ Int.* **51**, 945 (2011).
40. X. Quelennec and J. J. Jonas, *ISIJ Int.* **52**, 1145 (2012).